Iğdır Üniversitesi Fen Bilimleri Enstitüsü Dergisi, 12(4): 2140 - 2152, 2022
Journal of the Institute of Science and Technology, 12(4): 2140 - 2152, 2022
ISSN: 2146-0574, eISSN: 2536-4618
Fizik / *Physics* **DOI: 10.21597/jist.1118721**
Araştırma Makalesi / *Research Article*
Geliş tarihi / *Received*: 19.05.2022 **Kabul tarihi / *Accepted*: 24.09.2022**

Atıf İçin: Taşçıoğlu A, Yılmaz G, 2022. Atmosferik Koşullara Bağlı Olarak $CH_3NH_3PbI_3$ İnce Filmlerin Karanlık ve Fotoiletkenlik Davranışı. Iğdır Üniversitesi Fen Bilimleri Enstitüsü Dergisi, 12(4): 2140 - 2152.

To Cite: Tascioglu A, Yilmaz G, 2022. Dark and Photoconductivity Behavior of $CH_3NH_3PbI_3$ Thin Films Depending on Atmospheric Conditions. Journal of the Institute of Science and Technology, 12(4): 2140 - 2152.

Atmosferik Koşullara Bağlı Olarak $CH_3NH_3PbI_3$ İnce Filmlerin Karanlık ve Fotoiletkenlik Davranışı

Ayşegül TAŞÇIOĞLU[1], Gökhan YILMAZ[2*]

ÖZET: Metilamonyum kurşun iyodür ($MAPbI_3$) ($CH_3NH_3PbI_3$), başta fotovoltaik uygulamalar olmak üzere birçok alanda büyük potansiyele sahiptir. Ne yazık ki, $MAPbI_3$ ciddi şekilde bozunmadan muzdariptir. Bozunma sorunu, bu malzemenin fotovoltaik ve diğer potansiyel uygulamalarını sınırlandırmaktadır. Kararlı fotovoltaik malzeme üretebilmek için $MAPbI_3$'ün bozunma mekanizması ve elektronik kusur profilinin iletkenlik tarafında dikkatli bir şekilde anlaşılması gerekir. Bu çalışmada stres faktörlerinden kaynaklı elektronik kusur değişimleri incelenmiştir. $MAPbI_3$ filmler, termal kimyasal buhar biriktirme (Termal CVD) ve döndürmeli kaplama yöntemleri ile büyütülmüştür. Büyütme sıcaklıklarından kaynaklanan morfolojik farklılıklar, taramalı elektron mikroskobu (SEM) ile belirlenmiştir. Element analizler ve yapısal analizler, sırasıyla, enerji dağılımlı X-ışını spektroskopisi (EDS) ve X-ışını kırınımı (XRD) ile yapılmıştır. Depolanan $MAPbI_3$ filmleri, bozunma ve elektronik kusur değişikliklerini tanımlamak için vakum atmosferi, deiyonize su buharı (DIWV) atmosferi ve sabit sıcaklıkta (300 K) UV ışığı ile yaşlandırma gibi tek stres faktörlerine maruz bırakılmıştır. Numunelerin elektronik değişiklikleri zamana bağlı karanlık iletkenlik, sıcaklığa bağlı karanlık iletkenlik ve ışık akısına bağlı fotoiletkenlik ile incelenmiştir. Bu çalışma, iletkenlik tarafında $MAPbI_3$'ün bozunma mekanizması ve elektronik kusur profili hakkında derinlemesine bir anlayış sağlamaktadır

Anahtar Kelimeler: Metilamonyum kurşun iyodür, termal CVD, döndürerek kaplama, elektronik kusurlar, yarı-kararlılık

Dark And Photoconductivity Behavior of $CH_3NH_3PbI_3$ Thin Films Depending On Atmospheric Conditions

ABSTRACT: Methylammonium lead iodide ($MAPbI_3$) ($CH_3NH_3PbI_3$) has great potential for several fields, especially for photovoltaic applications. Unfortunately, $MAPbI_3$ can seriously suffer from degradation. Hence, the degradation problem limits the photovoltaic and other potential applications of this material. In order to produce a stable photovoltaic material, the degradation mechanism and electronic defect profile of $MAPbI_3$ should be understood carefully, especially regarding its conductivity. In this study, electronic defect changes due to stress factors were evaluated. $MAPbI_3$ films were deposited using thermal chemical vapor deposition (Thermal CVD) and spin coating techniques. Morphological differences due to deposition temperatures were defined by using scanning electron microscopy (SEM). Elemental analysis and structural analysis were conducted by energy-dispersive X-ray spectroscopy (EDS) and X- ray diffraction (XRD), respectively. Deposited $MAPbI_3$ films were exposed to in-situ stress factors such as vacuum atmosphere, deionized water vapor (DIWV) atmosphere, and UV light soaking at constant temperature (300 K) in order to define degradation and electronic defect changes. The electronic changes in the samples were investigated by time-dependent dark conductivity, temperature-dependent dark conductivity, and flux-dependent photoconductivity. This study provides an in-depth understanding of the degradation mechanism and electronic defect profile of $MAPbI_3$ regarding its conductivity.

Keywords: Methylammonium lead iodide, thermal CVD, spin coating, electronic defects metastability

[1] Ayşegül TAŞÇIOĞLU (**Orcid ID:** 0000-0002-1771-358X), Burdur Mehmet Akif Ersoy University, Agriculture, Livestock and Food Research Application and Research Center, Burdur, Türkiye

[2] Gökhan YILMAZ (**Orcid ID:** 0000-0003-0834-9736), Burdur Mehmet Akif Ersoy University, Faculty of Engineering and Architecture, Department of Energy Systems Engineering, Burdur, Türkiye

***Sorumlu Yazar/*Corresponding Author**: Gökhan YILMAZ, e-mail: gyilmaz@mehmetakif.edu.tr

INTRODUCTION

Organometal halide perovskites are a promising group of materials in many technological fields. Especially $MAPbI_3$ has cutting-edge technology applications such as light-emitting diodes (LEDs)(Tan et al., 2014; Cho et al., 2015), thin-film transistors (TFTs) (Wu et al., 2016), optically pumped lasers (Deschler et al., 2014), photodetectors (Moehl et al., 2014; Lin et al., 2015), resistive switching random access memory (ReRAM)(Gu and Lee, 2016), solar water splitting(Chen et al., 2015), and photovoltaic devices (Kojima et al., 2009). Of these application fields, probably the most popular one is the field of photovoltaics. There are many deposition techniques for perovskite deposition. The most popular ones are spin coating and spray pyrolysis. However, generally porous structures are formed in production with these methods (Girtan, 2020; Yilmaz 2021; Patil et al., 2012). Therefore, the Thermal CVD system and spin coating system were used together for perovskite production in this study. Recent studies on organometal halide perovskite ($MAPbI_3$) solar cells (perovskite solar cells, or PSCs) show that power conversion efficiency (PCE) starts at %3 and reaches %21. However, it was reported that in PSCs there are significant decreases in efficiency values after production (Noh et al., 2013). These decreases in efficiency with time are called aging, metastability, or instability. It has been alleged that the sources of these decreases are interfacial interactions and stress factors such as UV light, oxygen, and water vapor. When studies on the decrease in efficiency are investigated in detail, it is seen that the stress factor could not explain the outcome in detail if the measurements contained more than one stress factor at the same time (Bella et al., 2016; Pistor et al., 2016; Aristidou et al., 2015; Niu et al., 2015; Christians et al., 2015; Bass et al., 2014; You et al., 2014). Thus, it is not clear which stress factor is mainly related to degradation. In addition, it has been determined that the majority of the studies have been carried out on solar cells instead of layers. Another point is that the majority of the studies have been conducted on optical or structural degradation/change, instead of electrical change. Electrical degradation studies of the $MAPbI_3$ layer are very limited and it is not possible to compare the results due to the application of multiple stress factors. For this reason, it has become necessary to make the electrical measurements of the layer under the single stress factor condition.

In this study, absorption layers of PSCs ($MAPbI_3$ layers) were deposited by a two-step application thermal chemical vapor deposition (Thermal CVD) and the spin coating method on microscope glass. The structure and morphology of films were examined by X-ray diffraction (XRD) and Scanning Electron Microscopy (SEM) methods, respectively. By applying separately a single stress factor (vacuum atmosphere, high purity oxygen, deionized water vapor (DIW vapor), and UV light soaking), the conductivity changes in the material were determined by time-dependent dark conductivity, temperature-dependent dark conductivity, and flux-dependent photoconductivity. The degradation of $MAPbI_3$ films due to stress factors was examined in terms of meta/instability and tried to be understood in this study.

MATERIALS AND METHODS

Experimental Procedure

$MAPbI_3$ films were deposited on a glass substrate by a two-step application. The ***first step*** involves having 0.6 gr of lead iodide (PbI_2) (Sigma Aldrich %99) inserted in crucibles and deposited on a glass substrate by a Thermal CVD system. The thermal CVD evaporation is applied in a quartz tube pipe (diameter 5.0 $x10^{-3}$ m and length 6.0 $x10^{-2}$ m). In standard heat furnace systems, usually, a temperature sensor is placed inside the wall. In this study, a temperature sensor was placed inside the tube (nearby crucibles). Using this temperature measurement method, the real evaporation temperatures were defined

and measured in an accurate manner. In the Thermal CVD deposition procedure, the first tube was flushed (cleaned) with nitrogen (N_2) gas from undesirable gases before the deposition application. Subsequently, the tube was taken to vacuum conditions until a vacuum level of 10^{-3} mbar was reached. Following this step, starting from room temperature to deposition temperature, the tube was heated with the step of 10K per minute with the help of the Proportional Integrative Derivative (PID) control unit. After the system reached the deposition temperature, then Nitrogen gas was sent into the tube. Nitrogen gas was used as a transferring gas for evaporated sources with 200 sccm. Evaporation sources were kept at specific temperatures (693K and 613K) for 30 minutes during the evaporation process. After the deposition was completed, the system was left to cool by itself.

In the ***second step,*** methylammonium iodide (MAI) 0.2 gr (Sigma Aldrich %98) was dissolved with a 20ml 2-propanol and 5ml of solution deposited on the PbI_2 layer by a spin coater at 1300 rpm. The thin film production method is presented in figure 1. After deposition of $MAPbI_3$, the films were put on a hot plate under 80 ℃ for 1 minute. This procedure increased the crystallization of the thin film and made it dry. The details regarding the deposition temperature of PbI_2 films have been given in Table 1.

The thermal evaporation technique was used for the coplanar metal contact with a specific mask geometry configuration. Silver (Ag) was chosen as a metal contact on the surface of the $MAPbI_3$ film. The contact geometry parameter was chosen as 5.0 $x10^{-7}$ m, 5.0 $x10^{-7}$ m, and 5.0 x 10^{-4} m with respect to thickness, length, and gap. to thickness, length, and gap.

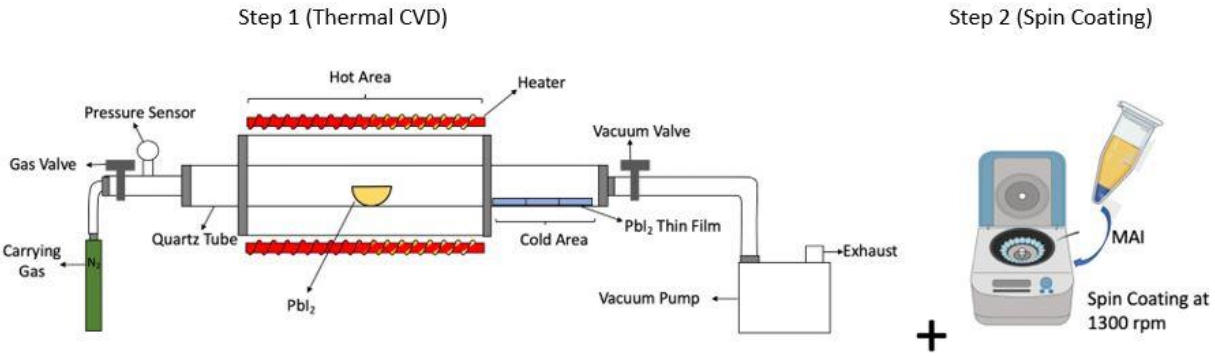

Figure 1. SEM images of the $MAPbI_3$ films at 5000x magnification a) 20T-SC-5 b) 20T-SC-6

Table 1. The deposition temperature detail of PbI_2 films

The Sample Code of $MAPbI_3$ films	PbI_2 evaporation temperature
20T-SC-5	693 K
20T-SC-6	613 K

The structural and morphological characterization of $MAPbI_3$ films were achieved by using XRD, EDS, and SEM respectively. The thickness of the samples was determined by SEM measurements from the cross-section of the films. $MAPbI_3$ film thicknesses were almost the same (~9.0 x 10^{-6} m). $MAPbI_3$ films were electrically characterized by time-dependent dark conductivity, temperature-dependent dark conductivity, and RT photoconductivity. Stress factors such as UV, oxygen, and DIW vapor were applied to $MAPbI_3$ films. Each stress factor was applied at 300K for 30 minutes. After stress factor application, the $MAPbI_3$ films were annealed under vacuum conditions. The annealing process was carried out to understand whether any change that occurred in the material was reversible or not. The cryostat was used for annealing applications between 300K to 400K under vacuum conditions.

Annealing was applied for 30 minutes at 400K under vacuum conditions. Subsequently, the $MAPbI_3$ films were left to cool off by themselves.

RESULTS AND DISCUSSION

Structural and Morphological Characterization

SEM measurements of the samples were conducted by using an FEI Quanta FEG 250 device. 5000x magnified SEM images of the $MAPbI_3$ films have been presented in Figure 2. In figure 2, small and large hexagon/triangle layers are stacked on top of each other to form random orientations. On the other hand, in figure 2 (b), the thin film consists of small and large crystal cubes. It can be seen that figure 2 (b) shows surface morphology that is more compact than figure 2 (a). It is also shown that the surface morphology of figure 2 (a) is more porous than figure 2 (b), due to the arbitrarily oriented hexagonal/triangle layers. It was clearly seen that; these layered structures create porosity on the surface of the material and increase the inner surface area of the material. It was seen that the porosity was more evident in the films produced only with the spin coating technique (Girtan, 2020). In addition, similar porosity situation was observed in silicon thin films. Hence, it was observed that when the structurally crystalline volume fraction begins to increase, then porosity and roughness also increase. (Houben et al., 1998). Energy-dispersive X-ray spectroscopy (EDS) measurements were conducted on ten different positions for each sample. Average atomic percentages of samples given have been provided in Table 2. In Table 2, all the related elements (C, H, N, Pb, and I) of $MAPbI_3$ films' are shown. Depending on the atomic percentages, a one-third ratio between PbI_2 and MAI was determined.

Bruker AXS D8 Advanced system and Cu tube were used for the XRD measurements and X-ray source. XRD measurements were conducted using the 2-theta scale between 0 to 70 degrees as shown in figure 3. As can be seen in figure 3, peaks are matching together and are similar to literature peak values for $MAPbI_3$ forms (Oku, 2015). In the sample 20T-SC-6, only 10-, 11-, and 52-degree peaks can be seen to be different as compared to 20T-SC-5. These peak values refer to PbI_2 crystalline formation (Condeles et al., 2006; Zhang et al., 2015; Silva Filho et al., 2019).

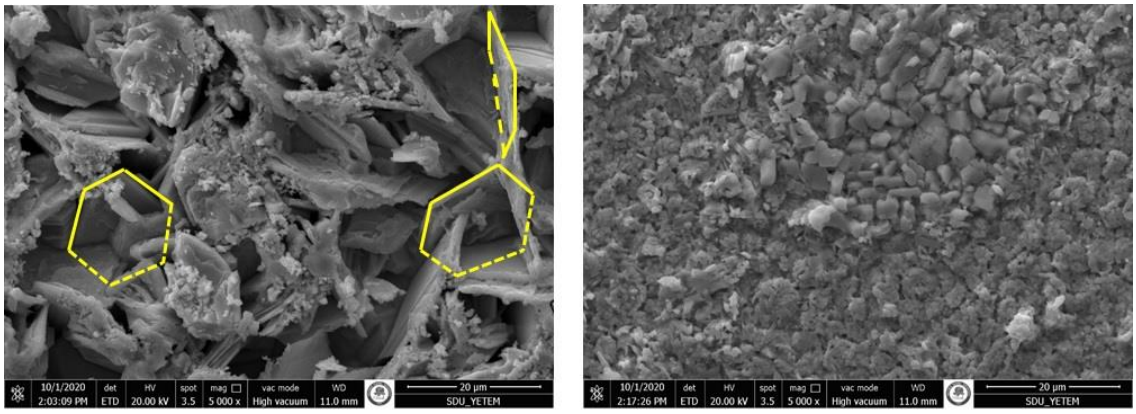

(a) (b)

Figure 2. MAPbI3 films SEM images at 5000x magnification a) 20T-SC-5 b) 20T-SC-6

Table 2. EDS measurement in atomic percentages of $MAPbI_3$ films

Element	20T-SC-6 Atomic (%)	20T-SC-5 Atomic (%)
C	33.30	34.96
N	32.26	24.76
Pb	5.10	8.62
I	29.34	31.66

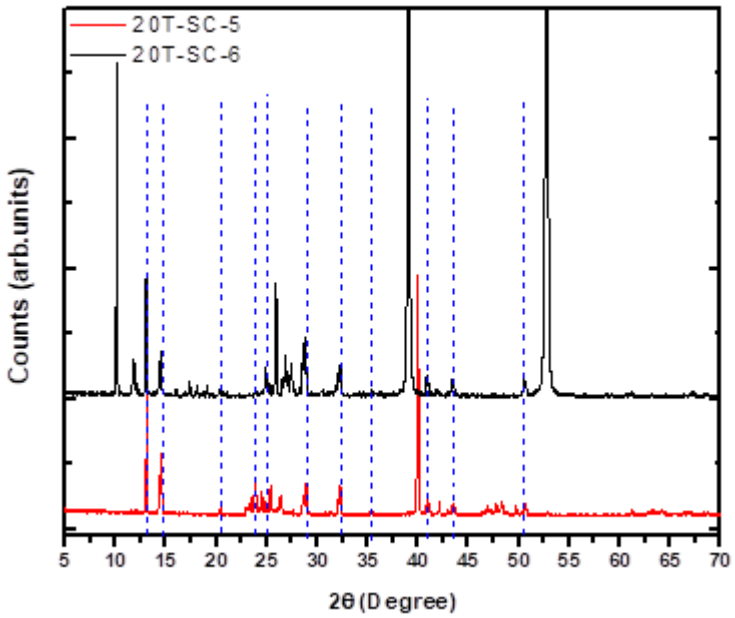

Figure 3. The XRD pattern of the films of samples 20T-SC-5 and 20T-SC-6 ($MAPbI_3$). Blue dashed lines were just inserted as an eye guide for matching the degrees

Electrical Characterization

In figure 4, UV aging and atmospheric transition change values have been provided. As seen in figure 4 (a) 20T-SC-6 shows a 6-times decrease in the dark conductivity values during the transition from laboratory atmosphere to vacuum conditions. On the other hand, it is seen that the dark conductivity value of the 20T-SC-5 increased by almost 2 times. The only reason for the change in the dark conductivity value during the transition from the laboratory atmosphere to the vacuum atmosphere was due to the gas molecules on the surface of the samples, which were removed from the environment by vacuum(Yilmaz et al., 2021). Although the 20T-SC-6 film had a more compact surface, it was much more affected by atmospheric gases than the 20T-SC-5. When samples reached a steady state condition in a vacuum atmosphere, an annealing procedure was applied between 300K to 400K. Annealing procedure was applied in order to understand whether the stress-factor-related conductivity change was reversible or not. After the first annealing, samples were cooled to 300K with PID. This state is called the annealed-1 state. At annealed-1 state, while in steady state condition in a vacuum atmosphere, the samples were exposed to UV aging for 30 minutes at 300K. In this way, all other unwanted conditions (moisture, atmospheric gases, different temperatures) were eliminated, and a single stress factor (for this case UV light) was applied to the samples. Figure 4 (b) shows UV aging time-dependent conductivity values. As can be seen in figure 4 (b), the sample 20T-SC-6's conductivity value was increased by almost 2 orders of magnitude due to the UV light. Similar behavior was also observed at different luminous fluxes produced by the xenon lamp (Girtan, 2020). When the UV light application was turned off, a 5-times decrease in the dark conductivity values was observed compared to the annealed-1 state. In figure 4 (b), the sample 20T-SC-5's conductivity value was increased by almost 1 order of magnitude because of the UV light. However, after the UV aging, 20T-SC-5's dark conductivity values were almost the same as the annealed-1 state values.

When the UV aging was finished, a second annealing cycle was applied to the samples. After that (at 300K, in a vacuum atmosphere, at steady state condition, in the dark) the high purity oxygen gas was transferred to the cryostat. All other unwanted stress factors such as moisture, light, other gasses, and different temperatures were eliminated. In this manner, only the oxygen could create an electronic defect

in the samples. Time-dependent measurements were carried out between the vacuum atmosphere to oxygen atmosphere transition. Figure 5 (a) shows dark conductivity changes with oxygen degradation. As can be seen in figure 5 (a), sample 20T-SC-6's dark conductivity values increase two times with oxygen. After 30 minutes of oxygen aging, the system was put into a vacuum condition. Even if the oxygen was removed from the environment with a vacuum, the dark conductivity value of 20T-SC-6 did not change and remained constant. In this manner, it is possible to state that the oxygen molecules were attached (chemically or physically) to the surface of the sample 20T-SC-6 (Aristidou et al., 2015).

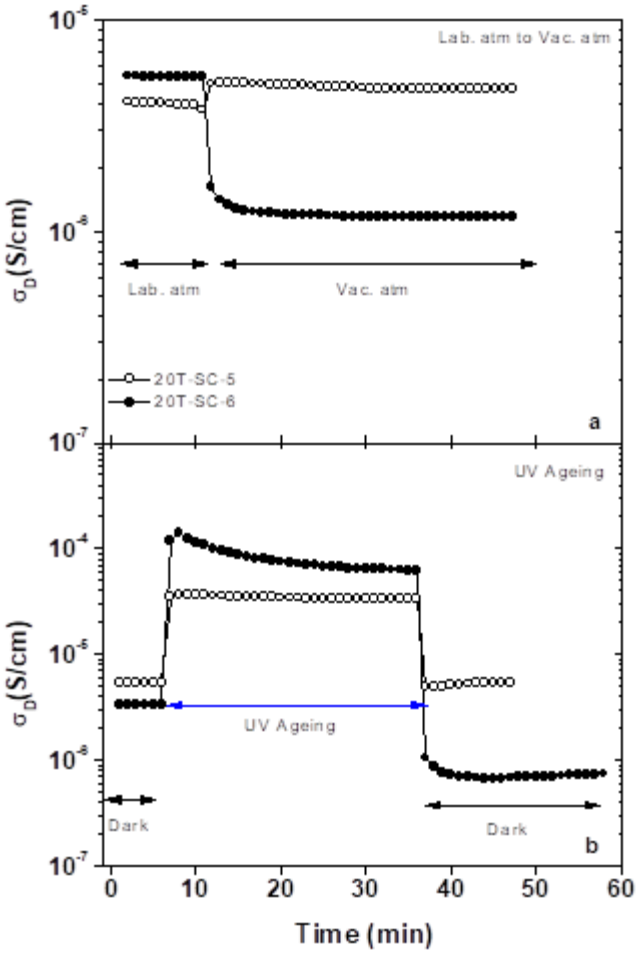

Figure 4. a) Laboratory atmosphere to vacuum atmosphere transition time-dependent dark conductivity **b)** UV aging time-dependent conductivity

The dark conductivity value of the sample 20T-SC-5 was decreased by a factor of 2 times due to oxygen aging. However, when the oxygen gas was removed from the environment by vacuum, the dark conductivity value returned to its first heat-treated value (annealed-1 state). This decrease in the conductivity and the return to its original state indicate that oxygen cannot make a bond in the thin film structure. Thus, this situation does not create a permanent conductivity change.

The dark conductivity changes of the samples due to DIW vapor is shown in figure 5 (b). It is clearly seen that the dark conductivity values of both samples were increased almost 10000 times because of the DIW vapor molecules. The DIW vapor molecules could stand between metal contacts and could create a parallel resistance effect. This situation has been visualized in figure 6. In this case, the resistance effect of water molecules R_2 is much lower than the materials' resistance R_1. Thus, the current prefers to flow through to DIW vapor molecules, thus dark conductivity values increase. This effect can be eliminated when the system is brought to vacuum atmosphere conditions. In this case, the

water molecules are removed from the environment, hence the current flows through the material. It is also known that long term humidity aging can change the structure of MAPbI3 (Christians et al., 2015).

In figure 5 (b) it can be seen that a sharp decrease was observed in the dark conductivity values after the system was brought to vacuum conditions. At a steady state in the vacuum atmosphere, the dark conductivity values of the sample 20T-SC-6 increased by 4 times with the DIW vapor application as compared to the annealed state. However, the dark conductivity values of the sample 20T-SC-5 were not changed with the DIW vapor application. It was observed to be the same with the annealed-2 state dark conductivity values.

After each stress factor, the photoconductivity values of the samples were measured depending on the flux. In Figures 7 and 8, the flux-dependent photoconductivity values of samples 20T-SC-5 and 20T-SC-6 have been presented. In figure 7 (a) after UV aging, photoconductivity values almost decreased two times as compared to the annealed-1 state. This indicated that UV aging created an electronic defect in the band-gap region. After the second annealing, the photoconductivity values matched with UV-aged state values in the low flux (10^{14} cm^{-2} s^{-1}) region. The photoconductivity value after heat treatment-2 coincides with the photoconductivity value after heat treatment-1 at the end of the middle luminous flux and high luminous flux regions (from 2.0x1015 cm^2 s^1 to 1017 cm^2 s^1). This shows that the second annealing created a partial recovery of the electronic defects, which were caused by UV aging. When oxygen was applied to the system, the photoconductivity values were decreased by almost two times. Oxygen-aged state photoconductivity values also matched with the UV-aged state photoconductivity values, which have been shown in figure 7 (b). In order to understand whether the oxygen aging was reversible or not, third annealing was applied. After the third annealing, photoconductivity values were not changed according to their oxygen-aged or UV-aged state. In this case, it can be stated that the oxygen also creates an electronic defect, especially in the middle and high flux (10^{16} cm^{-2} s^{-1} to 10^{17} cm^{-2} s^{-1}) region. DIW vapor-aged state photoconductivity values have been given in figure 7 (c) for sample 20T-SC-5. When DIW vapor aging was applied, the photoconductivity values decreased almost by one order of magnitude as compared to the annealed-1 state photoconductivity values. After the fourth annealing, this decrease in the photoconductivity was partially recovered, but still remained below the UV-aged state photoconductivity values.

In figure 8 (a) UV-light soaked state, annealed-1 state, and annealed-2 state photoconductivity values have been shown for the sample 20T-SC-6. In order to show it clearly, the UV aged state symbol was kept higher than the other state symbols. As can be seen in figure 8 (a), UV light-soaked state photoconductivity values decreased by almost a factor of 4 times as compared to the annealed-1 state values. After the second annealing, especially in the low flux (1014 cm-2 s-1) range, the photoconductivity values partially recovered. However, in the middle (1015 cm-2 s-1, 1016 cm-2 s-1) and high (1017 cm-2 s-1) flux range region, the annealed-2 state photoconductivity values were matching with the UV-aged state values. This result depicts that the UV-aging created an electronic defect in the sample. After oxygen application, the photoconductivity values increased until the annealed-1 state values, which have been shown in figure 8 (b). However, this photoconductivity increase was completely gone after the third annealing application, which means that the oxygen created a completely reversible degradation on the sample 20T-SC-6. It was also observed that the annealed-3 state photoconductivity values matched with the UV-aged state. In this case, it can be said that the oxygen did not create any additional electronic defect state in the sub-bandgap region of the sample 20T-SC-6. The same behavior was also observed after the DIW application in figure 8 (c). After the DIW application, the photoconductivity values increased until the annealed-1 state values were reached. On the other hand, photoconductivity values after the fourth heat treatment (annealing) returned to the

photoconductivity values obtained after UV aging. This shows that UV aging was responsible for the electronic irreversible degradation in the sample 20T-SC-6.

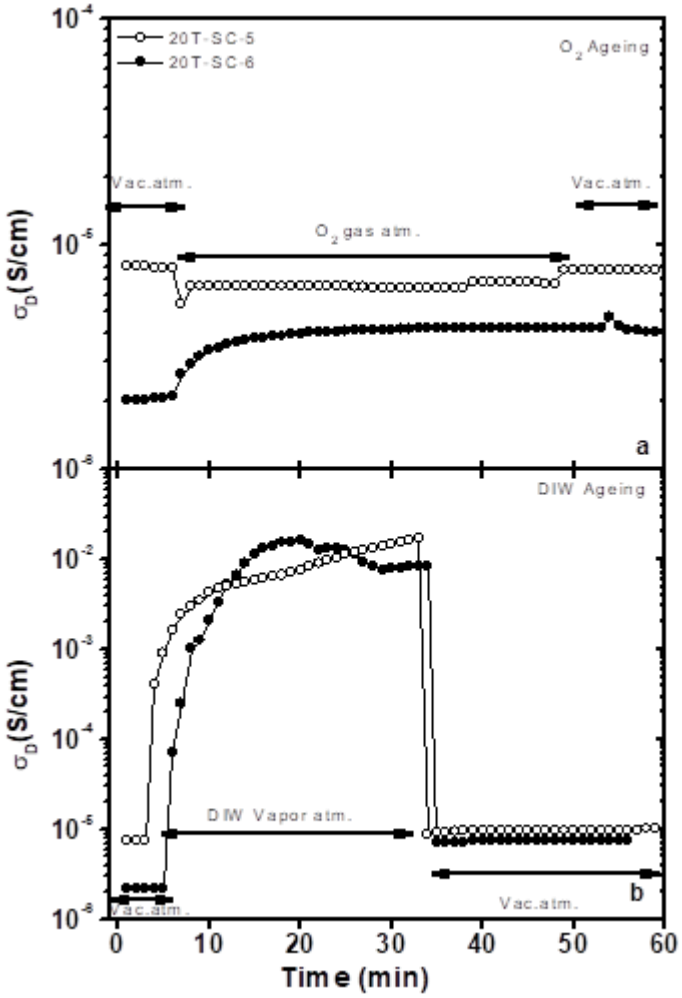

Figure 5. a) Oxygen aging time-dependent dark conductivity **b)** DIW aging time-dependent dark conductivity

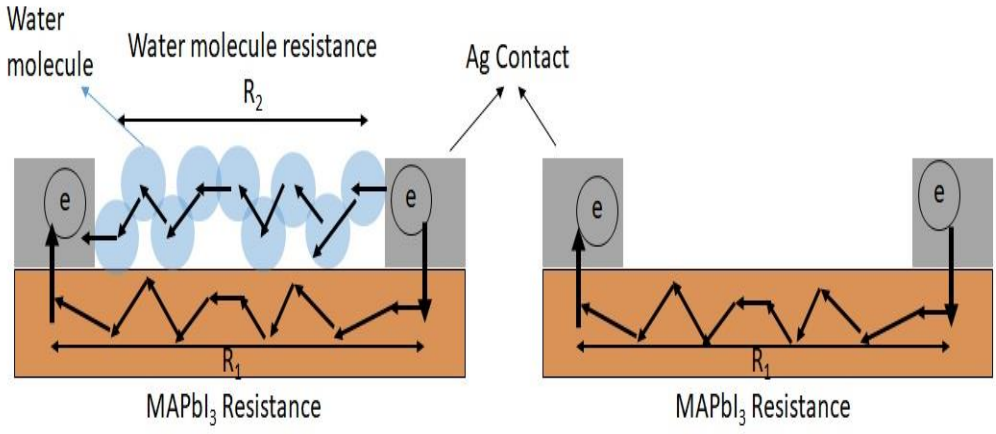

Figure 6. Schematic illustration of the parallel resistance effect

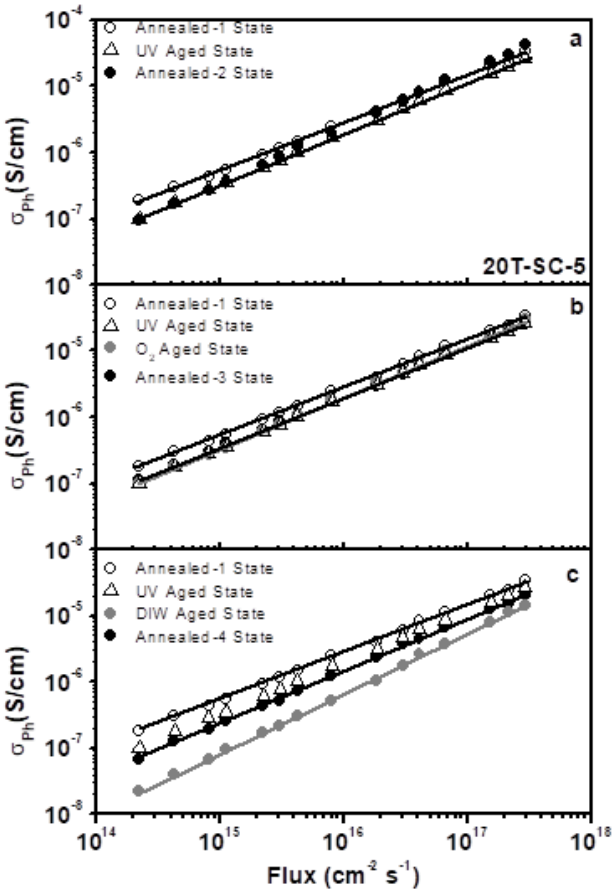

Figure 7. Sample 20T-SC-6 **a)** UV-light aged, **b)** Oxygen aged, **c)** DIW vapor aged temperature-dependent dark conductivity values

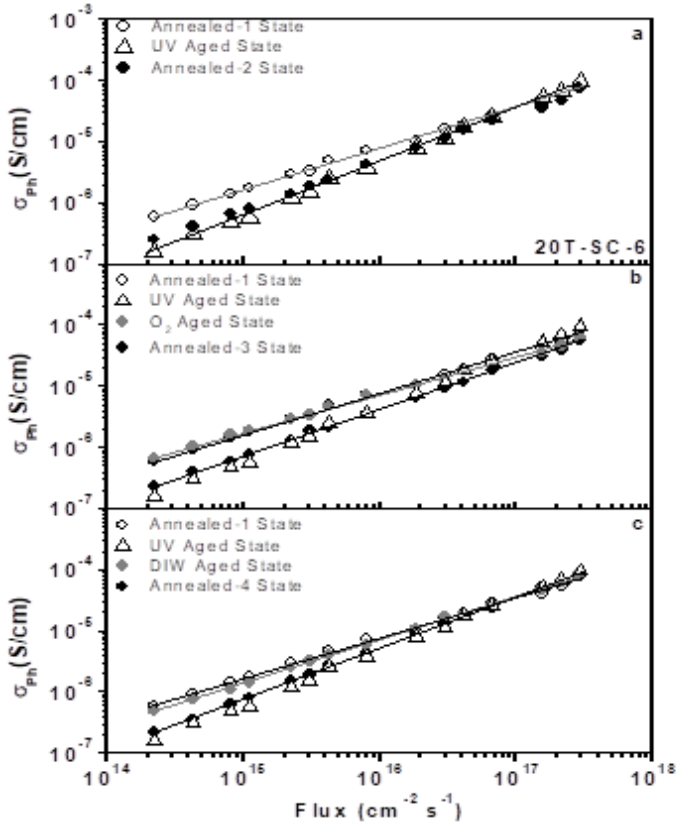

Figure 8. Sample 20T-SC-5 **a)** UV-light aged, **b)** Oxygen aged, **c)** DIW-vapor aged temperature-dependent dark conductivity values

Figure 9 shows the mobility-lifetime product (μτ) change depending on the stress factor application. Mobility-lifetime values were calculated depending on the photoconductivity and generation rate values (Yılmaz, 2021). As it can be seen in figure 9 (a), the μτ product values of the sample 20T-SC-5 decreased with the laboratory atmosphere aged state, annealed-1 state, and UV-aged state. The reduction in μτ product is evidence of an increase in the defect density because of atmospheric stress factors. After the UV-aged state, the μτ product values almost stayed constant until the DIW application. A sharp decrease in μτ product was observed with the DIW application, and this sharp decrease was partially recovered with the annealed-4 state. This situation shows that DIW aging can create a drastic increase in defects. However, this defect increase can be partially eliminated with an annealing application. In figure 9 (b), the μτ product values of the 20T-SC-6 samples increased depending on the laboratory-aged state with annealing. UV application creates a drastic decrease in the μτ product values. After the process of UV aging, there was an increase in the μτ product values. However, this μτ product values increase in an almost reversible manner with annealing procedures. The increase in the μτ product values is evidence of a decrease in the defect density caused by stress factors. Generally, the increase in the μτ product values could be the reason for the creation of defects, and the decrease in the μτ product values could be the reason for the passivation of defects.

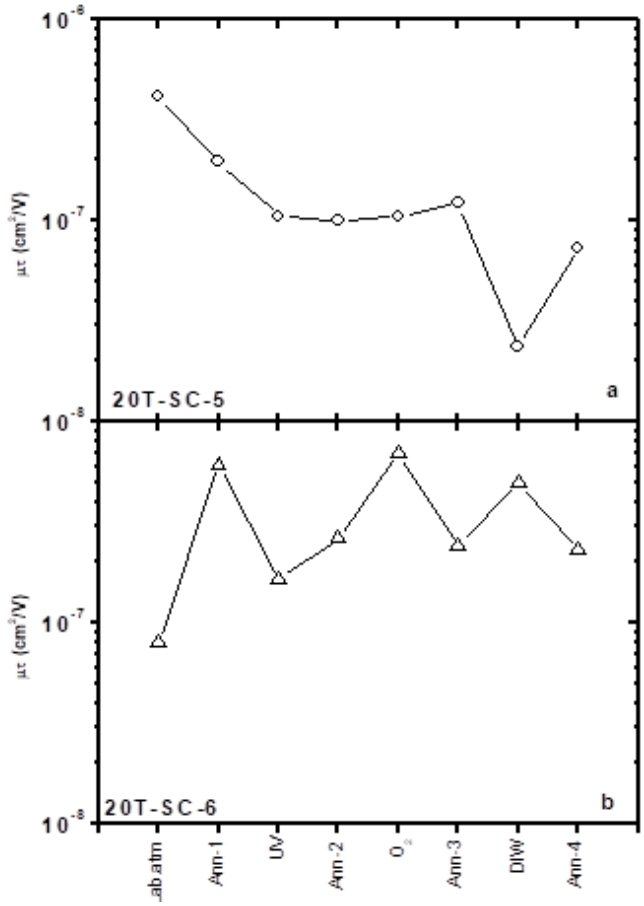

Figure 9. Mobility-lifetime product change depending on stress factors **a)** 20T-SC-5, **b)** 20T-SC-6 samples

CONCLUSION

The $MAPbI_3$ film layers were prepared by thermal CVD and spin coating techniques. The different deposition temperature of thermal CVD allows us to create a different morphology. We have determined the degradation process of $MAPbI_3$ in a laboratory atmosphere, an oxygen atmosphere, a DIW vapor

atmosphere, and in a UV-light soaking environment by time-dependent dark conductivity and photoconductivity. The samples, even when growth with the same technique, showed different dark and photoconductivity changes in the environment transitions such as from laboratory to vacuum, vacuum to oxygen, and vacuum to DIW vapor. The reason for the change in the dark conductivity values during the ambient change is the additional resistance effect, which was created by the molecules attached to the surface. Gas molecules such as moisture and oxygen can be attached physically to the surfaces of the samples. Those physically attached to the material surface between molecules can stay in place through Coulombic interaction, and these molecules can be removed from the surface with a vacuum application (Smirnov et al., 2004). The atmospheric changes in the sample 20T-SC-6, which were created by surface interaction, were observed with the dark conductivity values. On the other hand, the dark conductivity values of the sample 20T-SC-5 did not change dramatically. So, the sample 20T-SC-5 looks to be quite insensitive to gas molecules and atmospheric changes. However, UV-light soaking has a completely different aging mechanism (Abdelmageed et al., 2016; Mei et al., 2020; Watts, 2022). High energy photons (in the UV range) can break chemical bonds in the samples. Therefore, broken bonds create electronic defects in the band-gap region. The increase in the defects caused by stress factors creates a decrease in the $\mu\tau$ product values and a decrease in photoconductivity, as well as changes in the occupancy of localized states (Watss, 2022). On the other hand, the decrease in the defects caused by stress factors creates an increase in the $\mu\tau$ product values and this increase is the source of the increase in photoconductivity. Therefore, we can say that UV light and DIW vapor can mainly create electronic defects and changes the $\mu\tau$ product and photoconductivity values.

ACKNOWLEDGEMENTS

This study was funded by TUBITAK with Project number 119F033. This work is also supported by the Scientific Research Project Fund of Burdur Mehmet Akif Ersoy University under project numbers 2017K12 - 41003-12 and 0695-YL-21. The authors would like to give special thanks to Dr. Friedhelm FINGER and Jülich Research Center Germany. In addition, the authors would like to thank Ayşegül COŞKUN for helping with the measurements, Prof.Dr. Fatih Mehmet EMEN, Assoc. Dr. Murat KALELİ, and Dr.Salih AKYÜREKLİ for academic encouragement and their support

Conflict of Interest

The article authors declare that there is no conflict of interest between them.

Author's Contributions

The authors declare that they have contributed equally to the article.

REFERENCES

Abdelmageed G, Jewell L, Hellier K, Seymour L, Luo , Bridges F, Zhang J, Carter S, 2016. Mechanisms for light induced degradation in MAPbI3 perovskite thin films and solar cells. Appl. Phys. Lett. 109, 233905.

Aristidou, Nicholas, Irene Sanchez-Molina, Thana Chotchuangchutchaval, Michael Brown, Luis Martinez, Thomas Rath, and Saif A. Haque, 2015. The Role of Oxygen in the Degradation of Methylammonium Lead Trihalide Perovskite Photoactive Layers. Angewandte Chemie - International Edition 54 (28): 8208–12.

Bass, Kelsey K., R. Eric McAnally, Shiliang Zhou, Peter I. Djurovich, Mark E. Thompson, and Brent C. Melot, 2014. Influence of Moisture on the Preparation, Crystal Structure, and Photophysical Properties of Organohalide Perovskites. Chem. Commun. 50 (99): 15819–22.

Bella, Federico, Gianmarco Griffini, Juan-Pablo Correa-Baena, Guido Saracco, Michael Grätzel, Anders Hagfeldt, Stefano Turri, and Claudio Gerbaldi, 2016. Improving Efficiency and Stability of Perovskite Solar Cells with Photocurable Fluoropolymers. Science 354 (6309): 203–6.

Chen, Yong Siou, Joseph S. Manser, and Prashant V. Kamat, 2015. All Solution-Processed Lead Halide Perovskite-BiVO4 Tandem Assembly for Photolytic Solar Fuels Production. Journal of the American Chemical Society 137 (2): 974–81.

Cho, Himchan, Su Hun Jeong, Min Ho Park, Young Hoon Kim, Christoph Wolf, Chang Lyoul Lee, Jin Hyuck Heo, et al, 2015. Overcoming the Electroluminescence Efficiency Limitations of Perovskite Light-Emitting Diodes. Science 350 (6265): 1222–25.

Christians, Jeffrey A., Pierre A. Miranda Herrera, and Prashant V. Kamat, 2015. Transformation of the Excited State and Photovoltaic Efficiency of CH 3 NH 3 PbI 3 Perovskite upon Controlled Exposure to Humidified Air. Journal of the American Chemical Society 137 (4): 1530–38.

Condeles, J. F., R. C.Z. Lofrano, J. M. Rosolen, and M. Mulato, 2006. Stoichiometry, Surface and Structural Characterization of Lead Iodide Thin Films. Brazilian Journal of Physics 36 (2 A): 320–23.

Deschler, Felix, Michael Price, Sandeep Pathak, Lina E. Klintberg, David Dominik Jarausch, Ruben Higler, Sven Hüttner, et al, 2014. High Photoluminescence Efficiency and Optically Pumped Lasing in Solution-Processed Mixed Halide Perovskite Semiconductors. Journal of Physical Chemistry Letters 5 (8): 1421–26.

Mihaela Girtan 2020. On the electrical and photoelectrical properties of CH3NH3PBI3 perovskites thin films Solar Energy 195 446–453

Gokhan, Yilmaz, 2021. Creation and Investigation of Electronic Defects on Methylammonium Lead Iodide (CH3NH3PbI3) Films Depending on Atmospheric Conditions. The European Physical Journal D 75 (6): 174.

Gu, Chungwan, and Jang Sik Lee, 2016. Flexible Hybrid Organic-Inorganic Perovskite Memory. ACS Nano 10 (5): 5413–18.

Houben, L., M. Luysberg, P. Hapke, R. Carius, F. Finger, and H. Wagner. 1998. Structural Properties of Microcrystalline Silicon in the Transition from Highly Crystalline to Amorphous Growth. Philosophical Magazine A: Physics of Condensed Matter, Structure, Defects and Mechanical Properties 77 (6): 1447–60.

Kojima, Akihiro, Kenjiro Teshima, Yasuo Shirai, and Tsutomu Miyasaka, 2009. Organometal Halide Perovskites as Visible-Light Sensitizers for Photovoltaic Cells. Journal of the American Chemical Society 131 (17): 6050–51.

Lin, Qianqian, Ardalan Armin, Paul L. Burn, and Paul Meredith, 2015. Filterless Narrowband Visible Photodetectors. Nature Photonics 9 (10): 687–94.

Mei A., Sheng Y, Ming Y, Hu Y, Rong Y, Zhang W, Luo S, Na G, Tian C, Hou X, Xiong Y, Zhang Z, Liu S, Uchida S, Kim T, Yuan Y, Zhang L, Zhou, Y, Han H, 2020. Stabilizing Perovskite Solar Cells to IEC61215:2016 Standards with over 9,000-h Operational Tracking. Joule 4, 2646–2660

Moehl, Thomas, Jeong Hyeok Im, Yong Hui Lee, Konrad Domanski, Fabrizio Giordano, Shaik M. Zakeeruddin, M. Ibrahim Dar, et al, 2014. Strong Photocurrent Amplification in Perovskite Solar Cells with a Porous TiO2 Blocking Layer under Reverse Bias. Journal of Physical Chemistry Letters 5 (21): 3931–36.

Niu, Guangda, Xudong Guo, and Liduo Wang, 2015. Review of Recent Progress in Chemical Stability of Perovskite Solar Cells. Journal of Materials Chemistry A 3 (17): 8970–80.

Noh, Jun Hong, Sang Hyuk Im, Jin Hyuck Heo, Tarak N. Mandal, and Sang Il Seok, 2013. Chemical Management for Colorful, Efficient, and Stable Inorganic–Organic Hybrid Nanostructured Solar Cells. Nano Letters 13 (4): 1764–69.

Oku, Takeo, 2015. Crystal Structures of CH3NH3PbI3 and Related Perovskite Compounds Used for Solar Cells. In Solar Cells - New Approaches and Reviews, i:13. InTech.

Pistor, Paul, Alejandro Ruiz, Andreu Cabot, and Victor Izquierdo-Roca, 2016. Advanced Raman Spectroscopy of Methylammonium Lead Iodide: Development of a Non-Destructive Characterisation Methodology. Scientific Reports 6 (October): 1–8.

Silva Filho, José Maria Clemente da, Richard Landers, and Francisco Chagas Marques, 2019. Lead Iodide and Perovskite Films Obtained by Iodination of PbS Thin Films. Journal of Inorganic and Organometallic Polymers and Materials 29 (6): 2161–67.

Smirnov, V., S. Reynolds, C. Main, F. Finger, and R. Carius, 2004. Aging Effects in Microcrystalline Silicon Films Studied by Transient Photoconductivity. Journal of Non-Crystalline Solids 338–340 (June): 421–24.

Tan, Zhi-Kuang, Reza Saberi Moghaddam, May Ling Lai, Pablo Docampo, Ruben Higler, Felix Deschler, Michael Price, et al, 2014. Bright Light-Emitting Diodes Based on Organometal Halide Perovskite. Nature Nanotechnology | 9.

Wu, Yuxiang, Juan Li, Jian Xu, Yangyang Du, Like Huang, Jian Ni, Hongkun Cai, and Jianjun Zhang, 2016. Organic-Inorganic Hybrid CH3NH3PbI3 Perovskite Materials as Channels in Thin-Film Field-Effect Transistors. RSC Advances 6 (20): 16243–49.

Yilmaz, Gokhan, Aysegul Cosgun, and Aysegul Tascioglu, 2021. Lead Iodide Thin-Film Morphological-Dependent Metastability Investigation by Electrical Conductivity. Journal of Materials Science: Materials in Electronics 32 (3): 3222–31.

You, Jingbi, Ziruo Hong, Tze Bin Song, Lei Meng, Yongsheng Liu, Chengyang Jiang, Huanping Zhou, Wei Hsuan Chang, Gang Li, and Yang Yang, 2014. Moisture Assisted Perovskite Film Growth for High Performance Solar Cells. Applied Physics Letters 105 (18).

Watts C Lowell, 2022. Light Soaking in Metal-halide Perovskites. Oregon State University. PhD Dissertation.

Zhang, Wei, Michael Saliba, David T. Moore, Sandeep K. Pathak, Maximilian T. Hörantner, Thomas Stergiopoulos, Samuel D. Stranks, et al, 2015. Ultrasmooth Organic-Inorganic Perovskite Thin-Film Formation and Crystallization for Efficient Planar Heterojunction Solar Cells. Nature Communications 6 (1): 6142.